Journal of the European Ceramic Society 46 (2026) 117927

Contents lists available at ScienceDirect

Journal of the European Ceramic Society

journal homepage: www.elsevier.com/locate/jeurceramsoc

Development of mid-infrared-transmitting cryolite ceramics via a cold sintering process below 200 °C

Natsuki Sato [a,b], Tatsuro Yoshioka [a], Tomohiro Kitagaki [a], Yeongjun Seo [b], Tomoyo Goto [b,c], Sunghun Cho [b], Tohru Sekino [b,*]

[a] Electric Works Company, Panasonic Corporation, 1048 Kadoma, Kadoma, Osaka 571-8686, Japan
[b] SANKEN, The University of Osaka, 8-1 Mihogaoka, Ibaraki, Osaka 567-0047, Japan
[c] Graduate School of Science and Technology, Nara Institute of Science and Technology, 8916-5 Takayama-cho, Ikoma, Nara 630-0192, Japan

ARTICLE INFO

Keywords:
Cold sintering
Ceramics
Cryolite
Infrared
Transmission

ABSTRACT

This study demonstrates, for the first time, the successful fabrication of mid-infrared-transmitting cryolite (Na_3AlF_6) ceramics via a cold sintering process (CSP) below 200 °C. Cryolite powders were synthesized by the solution precipitation and followed thermal treatment to control particle size ranging from 140 nm to 1.5 μm and moisture content that effects on the IR transmittance. Bulky dense cryolite ceramics could be obtained by the CSP using optimized synthesized cryolite powders. The resulting ceramics achieved high relative density (~90 %) and IR transmittance (over 80 % at 1 mm thickness) in the 3.8–5.6 μm wavelength range although relatively low sintering temperature below 200 °C. Furthermore, it was clarified that a critical balance exists between pore size and hydroxyl content for the transmission properties of cryolite ceramics. The present findings thus establish a sustainable, low-temperature route for producing optical fluoride ceramics suitable for infrared applications.

1. Introduction

Infrared (IR) radiation, an essential part of the electromagnetic spectrum, is commonly categorized into three regions based on wavelength: near-infrared (0.8–2.5 μm), mid-infrared (2.5–50 μm), and far-infrared (50–1000 μm). IR-transparent materials are crucial for applications such as windows, filters, and lenses in optoelectronic technology [1,2]. These materials include single-crystal materials, polycrystalline ceramics, and glass materials, each of which is selected based on specific application requirements. The fabrication of IR-transparent materials typically involves high-temperature processing. For instance, the production of single-crystal materials such as sapphire and silicon, as well as sintered ceramics such as translucent alumina and spinel, requires prolonged high-temperature treatment, leading to significant energy consumption [3–6]. Developing methods to manufacture IR-transparent materials at lower temperatures could significantly reduce the environmental impact associated with their production.

In recent years, low-temperature sintered ceramics have been actively investigated [7–9]. An example of such technology is the method known as the cold sintering process (CSP) [10]. This technique involves heating and pressurizing a mixture of ceramic raw material powder and a solvent (such as water, an acid, or basic solution) capable of dissolving the ceramic material at temperatures of approximately 400 °C or lower. This process induces the dissolution of inorganic raw particles and reprecipitation associated with the evaporation of the solvent. This transient liquid can partially dissolve the surface of the particles, which then re-precipitates at the points of contact, facilitating bonding between the particles. The CSP technique presents numerous advantages over conventional high-temperature sintering methodologies, including diminished energy consumption and the potential for enhanced material properties. Recent investigations have demonstrated the successful application of cold sintering to a diverse array of ceramic materials encompassing both oxides and non-oxides, thereby expanding the scope of this innovative approach.

CSP has been utilized to develop materials that demonstrate excellent transparency in both the visible and near-IR light spectra. For example, Guo et al. reported that sintering CaF_2 using CSP at 350 °C achieved a transmittance of up to approximately 85 % from visible light to approximately 1100 nm in the near-IR region [11]. Similarly, Liu et al. developed transparent materials for visible to near-IR wavelengths of up to approximately 2000 nm for BaF_2 [12] and 2700 nm for LiF [13] using CSP at a sintering temperature of 150 °C. Thus, there are several

* Corresponding author.
E-mail address: sekino@sanken.osaka-u.ac.jp (T. Sekino).

https://doi.org/10.1016/j.jeurceramsoc.2025.117927
Received 10 April 2025; Received in revised form 10 October 2025; Accepted 24 October 2025
Available online 26 October 2025

reports on the low-temperature sintering of transparent materials for wavelengths ranging from visible to near-IR below 2700 nm. However, low-temperature densification of IR-transparent materials that can transmit wavelengths longer beyond 2700 nm via CSP is challenging because of the key factors inhibiting IR transmission, specifically light scattering and absorption. Light scattering is predominantly caused by porosity, which significantly reduces the transmittance. On the other hand, absorption is influenced by the presence of hydroxyl groups and adsorbed water. These impurities exhibit absorption bands in the IR region owing to OH stretching [14] and HOH bending vibrations [15]. Although high-temperature sintering typically eliminates surface hydroxyl groups and adsorbed water in low-temperature sintering, they are more likely to remain in the sintered body [16]. As a result, residual hydroxyl groups and water can significantly reduce the IR transmittance.

To enhance the transmittance, it is essential to minimize scattering by reducing the pore size and suppressing absorption by effectively lowering the number of hydroxyl groups and adsorbed water. In sintered ceramics, pores are formed between densely packed particles of raw material. The particles are assumed to be ideal spheres. According to H. S. Field's close-packing theory, the largest sphere that can occupy the interstitial spaces has a maximum radius of 0.414 R, where R is the radius of the packed particles [17]. This suggests that the gap size between particles is proportional to the particle size. Therefore, reducing the particle size effectively decreases the pore size, which helps to suppress light scattering in ceramics. However, reducing the particle size also increases the specific surface area, which in turn increases the number of surface hydroxyl groups and adsorbed water. As previously mentioned, they tend to remain in the sintered body when processed at lower temperatures. Thus, careful design of the raw material particle size is essential to balance the reduction in both light scattering and absorption.

Based on the above reasons, the desired materials for IR transparency should have a long IR cutoff wavelength, a low refractive index, and minimal refractive index anisotropy to reduce scattering coefficients. Therefore, cryolite (Na_3AlF_6) was selected as the target material for the low-temperature sintering in this study. Cryolite is commonly used as a solvent for alumina in aluminum electrolysis [18,19]. It has a relatively long IR cutoff wavelength because of the energy absorption associated with phonon excitation of its intrinsic lattice vibrations, which occur at approximately 12.5 μm (the absorption edge is 800 cm^{-1}) [20,21]. Additionally, cryolite has a low average refractive index ($n_{av} \approx 1.337$) [22], which is particularly low among inorganic materials, and the refractive index difference (Δn_g) across different crystal orientations is less than 0.0015 [23], making it suitable for reducing light scattering.

In this study, we report the fabrication of cryolite ceramics with IR transparency at wavelengths above 2700 nm using cold sintering. Cryolite particles of different sizes were synthesized to control the pore size of the ceramics. A mixture of cryolite particles and water was densified at temperatures below 200 °C under applied pressure. To optimize the densification process, we investigated the effects of sintering temperature, uniaxial pressure, and duration time. We also examined the relationship between the raw material particle size and pore size in the ceramics to maximize IR transmittance. Previous studies have demonstrated the fabrication of cryolite ceramics by conventional high-temperature sintering at 640 °C [24,25]. However, to the best of our knowledge, this is the first report on the low-temperature sintering of cryolite ceramics and IR-transparent materials with wavelengths exceeding 2700 nm.

2. Material and methods

2.1. Synthesis of cryolite particles

Cryolite raw powder was synthesized following the procedure outlined in equation (i), which is based on the synthesis method for neighborite ($NaMgF_3$) [26].

$$6NaF + AlCl_3 \rightarrow Na_3AlF_6 + 3NaCl\ldots \quad (i)$$

Initially, NaF (FUJIFILM Wako Pure Chemical Corporation, Osaka, Japan) and aluminum chloride hexahydrate ($AlCl_3{\cdot}6\ H_2O$, FUJIFILM Wako Pure Chemical Corporation, Osaka, Japan) were dissolved in deionized water to prepare aqueous solutions of 768 and 640 mM, respectively. While stirring with a magnetic stirrer, 50 mL of aluminum chloride solution (at room temperature) was gradually added to 250 mL of sodium fluoride solution (also at room temperature), and the mixture was stirred for 3 h. The mixed solution was filtered through a membrane filter with a pore size of 200 nm to separate the solid from the liquid. To remove the byproduct, sodium chloride (NaCl), the filter cake was washed with deionized water after filtration. The collected cake was dried at 200 °C, ground using an agate mortar, and pulverized into a fine powder. Subsequently, to adjust the particle size, the powder was subjected to calcinate at temperatures ranging from 300 to 600 °C, resulting in cryolite powders with various particle sizes.

2.2. Sintering of cryolite particles

The synthesized cryolite raw powder was combined with deionized water, placed into an 8 mm diameter mold, and then heated and pressurized at temperatures below 200 °C using a press machine with hot plates to form disc-shaped cryolite-sintered ceramics. The sintering temperature was defined by the temperature settings of the press machine's upper and lower hot plates. Subsequently, the samples were dried at 200 °C. The amount of deionized water added ranged from 0 to 50 wt%, the sintering temperature varied between 120 and 200 °C, the uniaxial pressure was set between 195 and 780 MPa, and the duration time was between 5 and 60 min. To investigate the effect of adding deionized water during the sintering process, a sample was prepared under conditions where deionized water was not added. To investigate the effect of pressure, a sample was prepared by heating under representative sintering conditions (180 °C, 10 min, 10 wt% deionized water) without applying pressure, i.e., without placing the upper mold.

2.3. Characterization

The synthesized cryolite raw powder was characterized by X-ray diffraction (XRD, MiniFlex, Rigaku Co., Ltd., Tokyo, Japan) for crystal structure analysis, thermogravimetric-differential thermal analysis (TG-DTA, STA 2500 regulus, NETZSCH Geratebau GmbH, Selb, Germany) for thermal analysis, scanning electron microscopy (SEM, VE-9800, KEYENCE CORPORATION, Osaka, Japan) for particle morphology observation, and nitrogen adsorption-desorption (BELSORP MAX, MicrotracBEL Corp., Osaka, Japan) for specific surface area measurements. The specific surface area was determined using the Brunauer-Emmett-Teller (BET) method. The bulk densities of the fabricated sintered bodies were calculated from their weights and volumes. The IR transmittance was measured using a Fourier-transform IR spectrometer (FT-IR, IR-Tracer-100, Shimadzu Corp., Kyoto, Japan). To investigate changes in crystal structure and thermal behavior due to sintering, the fabricated cryolite ceramics were ground into powder using an agate mortar. XRD and TG/DTA measurements were then performed on the ground powders using the same procedures as those applied to the raw powders. Additionally, cross-sections of the sintered ceramics were processed using a cross polisher (CP, IB-9020CP, JEOL Ltd, Tokyo, Japan) with Ar gas, operating at 2–6 kV, and the polished surface was observed using field-emission scanning electron microscopy (FE-SEM, SU9000, Hitachi High-Tech Corp., Tokyo, Japan) to investigate the internal structure of the sintered ceramics. Using ImageJ software, we calculated the pore size of the cryolite ceramics from the cross-sectional FE-SEM images. First, the cross-sectional FE-SEM images were binarized to distinguish between cryolite and pore regions. Next, the "Particle

Analysis" function was used to analyze the pore area distribution from the binarized images. Furthermore, the equivalent circular diameter and pore size distribution of the pores were calculated from the pore area distribution [27], and the mean pore diameter d50 was determined.

3. Results and discussion

3.1. Preparation of the cryolite powders

XRD analysis was conducted to investigate the phase compositions of the synthesized powders before and after the calcination (Fig. 1). As shown in Fig. 1, although minor peaks attributed to the impurity phase $Na_5Al_3F_{14}$ were observed, the main peaks corresponded to the desired cryolite-phase Na_3AlF_6, confirming that cryolite was the primary phase in the synthesized powders. A trend of increasing peak intensity corresponding to the $Na_5Al_3F_{14}$ phase was observed as the calcination temperature increased. The melting point of cryolite has been reported to be approximately 1000 °C [28], making it improbable that cryolite undergoes a compositional change to form $Na_5Al_3F_{14}$ during calcination up to 600 °C. Before calcination, particles might include uncrystallized areas that could crystallize during thermal processing. Therefore, TG-DTA measurements were performed to study the crystallization behavior of the synthesized particles under calcination.

Fig. 2 shows the TG and DTA curves of the synthesized cryolite powders before and after calcination at 300 and 400 °C. The TG curves indicated that the weight of the synthesized cryolite powder gradually decreased upon calcination up to 550 °C, irrespective of the specific calcination temperature. However, within the range up to 400 °C, the degree of weight loss tended to decrease as the calcination temperature increased. The DTA curves exhibited a broad endothermic reaction in the temperature range up to 550 °C. The endothermic reaction accompanied by weight loss is considered to be due to dehydration, suggesting the release of water or hydroxyl groups within or on the surface of the particles during calcination. Additionally, the powders before calcination and those calcined at 300 °C exhibited weak exothermic peak at 350–400 °C. Given that the XRD peaks of $Na_5Al_3F_{14}$ increased with calcination above 300 °C, this exothermic peak was presumed to be associated with the crystallization of $Na_5Al_3F_{14}$.

To investigate the changes in particle size of synthesized cryolite powder with varying calcination temperatures, SEM observations and BET specific surface area measurements using nitrogen adsorption-desorption method were conducted on the raw powder. Fig. 3 presents the SEM images of the synthesized cryolite powder and a graph of particle size versus calcination temperature derived from BET specific surface area. Particle size was calculated using equation (ii) [29], assuming the particles are non-porous and spherical.

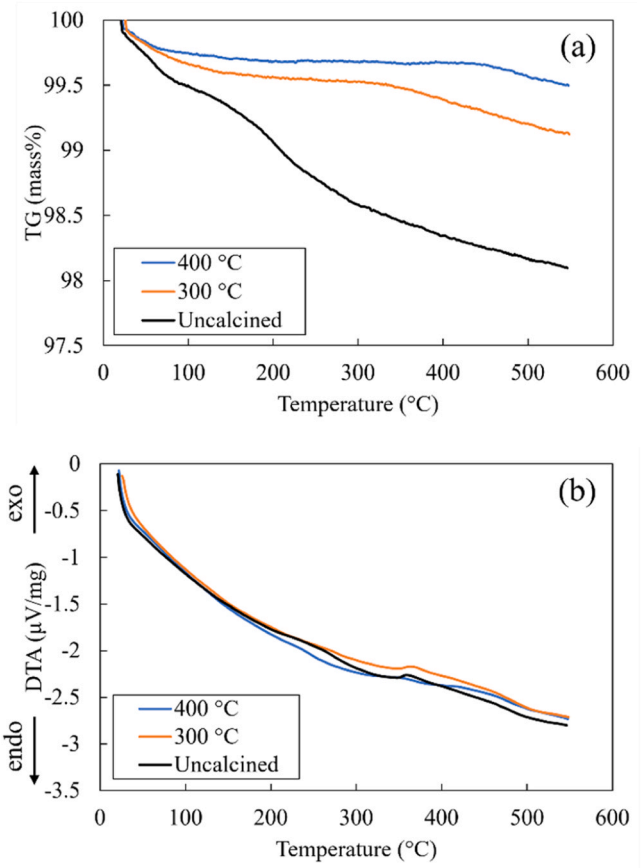

Fig. 2. (a) TG and (b) DTA curves of synthesized cryolite particles either uncalcined or calcined at 300 °C and 400 °C.

$$d = 6\times 10^3/(\rho\cdot S)\ldots \quad \text{(ii)}$$

Here, d represents particle diameter (nm), ρ is density (g/cm^3), and S is specific surface area (m^2/g). SEM images revealed that the particles are non-porous and irregularly shaped, with particle size increasing as calcination temperature rises. The particle size changes derived from BET specific surface area measurements also matched the SEM observations, showing that particle size tends to increase with higher calcination temperatures. Significant particle growth was particularly observed above 300 °C, suggesting that smaller particles coalesced

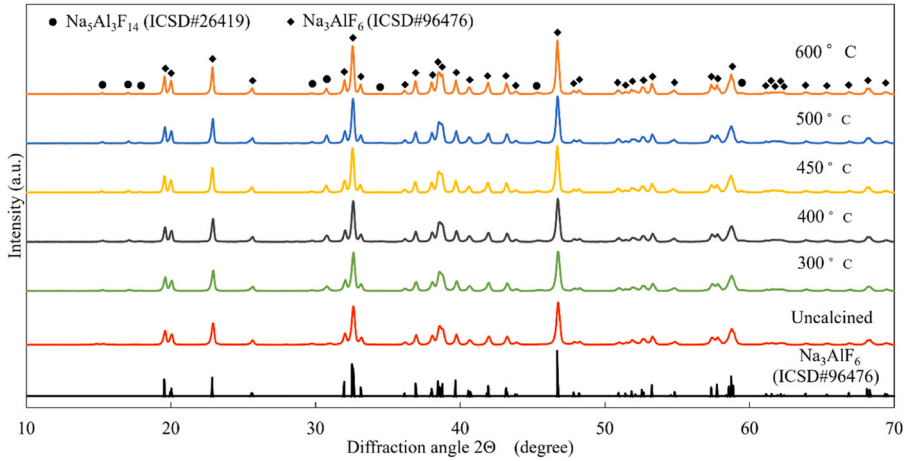

Fig. 1. XRD patterns of synthetic cryolite particles either uncalcined or calcined at various temperatures.

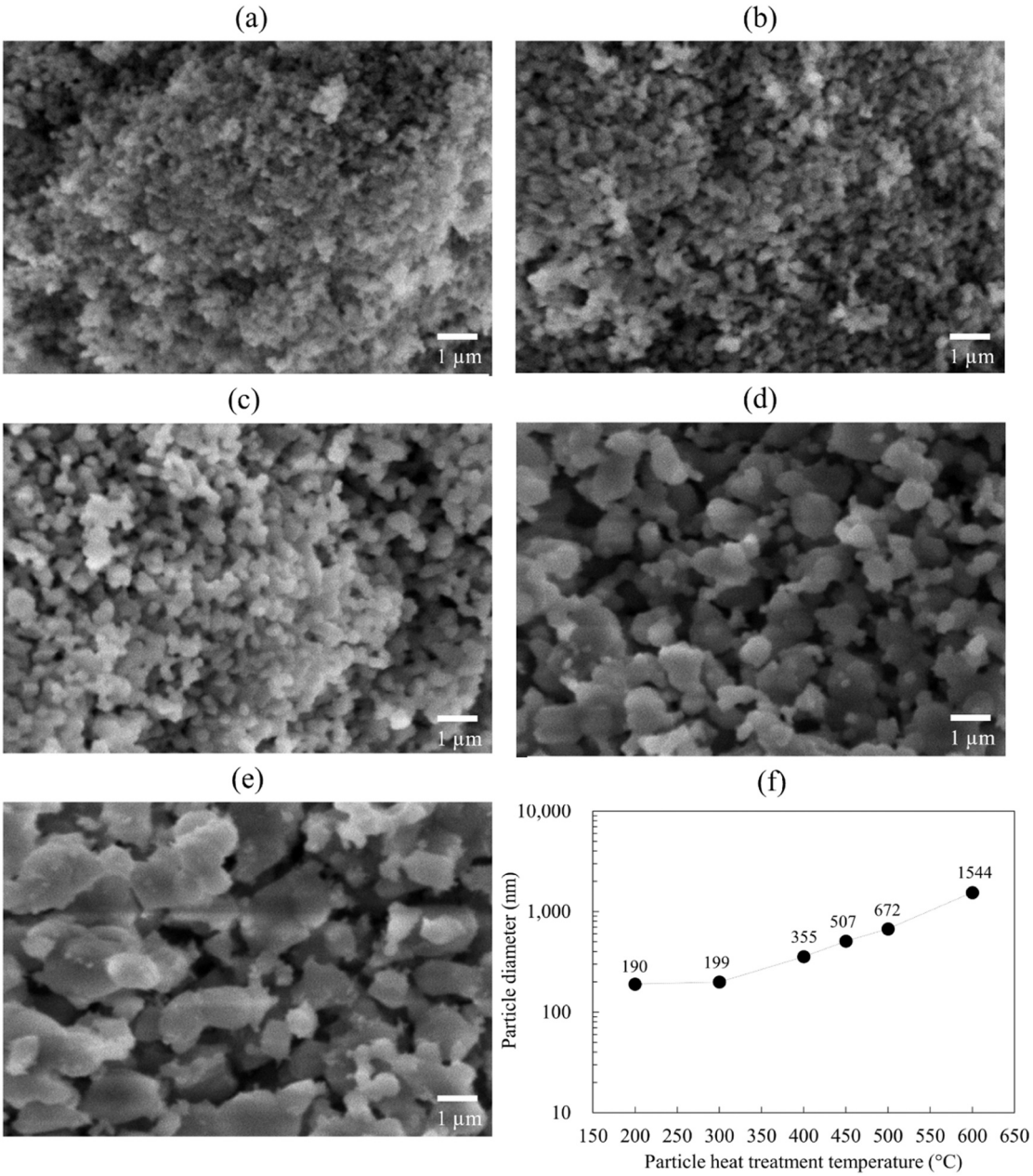

Fig. 3. SEM images of the synthesized cryolite powder, showing (a) particles either uncalcined or calcined at (b) 300 °C, (c) 400 °C, (d) 500 °C, and (e) 600 °C, and (f) a graph of particle size versus calcination temperature derived from BET specific surface area.

during heating.

3.2. *Densification and IR-transmittance of cryolite ceramics fabricated via CSP*

XRD measurements were conducted on the ground powders of the fabricated ceramics to investigate the compositional changes caused by CSP. Fig. 4 shows the XRD patterns of the ground powders from the cryolite ceramics fabricated using raw particles subjected to different calcination temperatures. The fabrication process conditions were standardized at a sintering temperature of 180 °C, uniaxial pressure of 585 MPa, duration time of 10 min, and addition of 10 wt% deionized water. The CSP optimization process is described later in the text (see the discussion of Fig. 9). Regardless of the raw particles used, the ceramics obtained primarily consisted of the target cryolite phase despite the presence of secondary phases. Compared with the XRD patterns of the raw powders shown in Fig. 1, the sample using uncalcined raw powder exhibited increased peaks of the secondary phase $Na_5Al_3F_{14}$. While crystallization of the secondary phase occurred at temperatures above 300 °C during the particle calcination, it proceeded at lower temperatures during the low-temperature sintering process. To investigate the cause of this crystallization behavior, a comparative sample was also prepared using the same uncalcined raw powder, following the same procedure as CSP except without applying pressure. Fig. 5 represents the XRD patterns of the raw powder (uncalcined), the ceramics sample fabricated from same uncalcined powder without pressure, and the sample processed by CSP. The sample heated without pressure did not show crystallization of secondary phases, whereas the CSP sample exhibited clear crystallization. This suggests that the temporary hydrothermal environment within the mold during the CSP promotes reactions more effectively than the atmosphere, reducing the crystallization temperature.

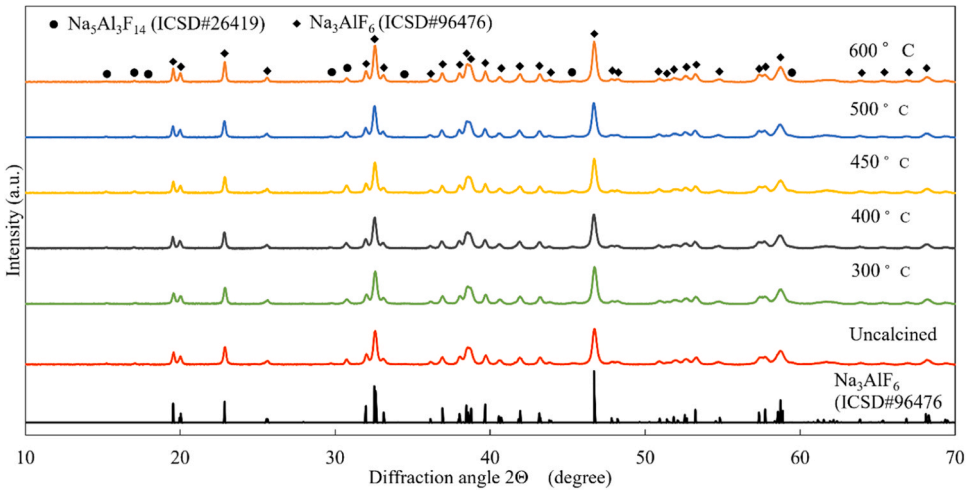

Fig. 4. XRD patterns (CuKα) of cryolite ceramics fabricated via the CSP method, using raw particles either uncalcined or calcined at various temperatures.

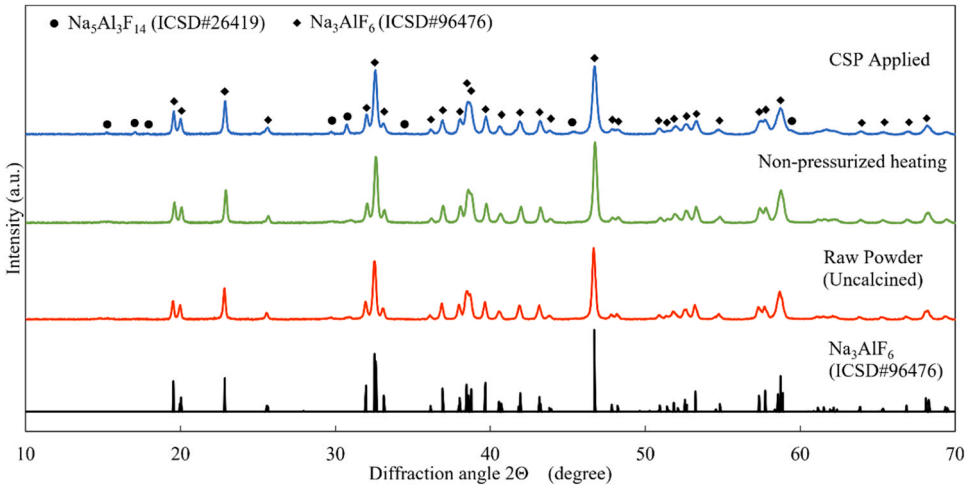

Fig. 5. XRD patterns (CuKα) of the uncalcined cryolite raw powder, and cryolite ceramics samples prepared from the same uncalcined powder either by heating without pressure or by CSP.

Fig. 6 shows cross-sectional FE-SEM images and binarized images of the cryolite ceramics with raw powder subjected to different calcination temperatures. To investigate the relationship between the particle size of the raw powder and the pore size within the ceramics, the pore size was determined from the cross-sectional FE-SEM images of the ceramics. Additionally, Fig. 7 illustrates the relationship between the particle diameter of the raw powder and the equivalent circular diameter, d50, of the pores within the ceramics, as analyzed from the binarized images. A reference line based on H.S. Field's close-packing theory [17] is also included, representing the theoretical maximum pore diameter between ideal spherical particles. It was observed that with an increase in the particle size of the raw powder (i.e., an increase in the calcination temperature), the pore size within the ceramics also tended to increase. Notably, when the calcination temperature was increased from 500 to 600 °C, there was a significant increase in both the particle and pore sizes. Perfectly spherical particles with uniform size would result in voids proportional to the particle size, and the pore size would also be proportional to the particle size (see Fig. 7). However, in ceramics manufactured with synthesized cryolite, the pore size increased with the particle size, showing a linear relationship with an intercept, differing from the strictly linear trend observed with the spherical particles. This discrepancy arises because the synthesized particles have a particle size distribution and irregular shapes, rather than being perfectly spherical. A broad particle size distribution allows smaller particles to occupy the gaps between larger particles, resulting in improved packing density [30]. Additionally, the non-ideal spherical shape of the particles results in a packing structure that deviates from the ideal state. As a result, the formation of a pore structure different from the ideal state is anticipated, such as pore coarsening due to pore connectivity. These factors are considered to cause the deviation from the direct proportionality between particle size and pore size.

It should be noted that the raw material particle size was indirectly estimated by assuming spherical particles based on the specific surface area obtained via the BET method. This approach involves several uncertainties. In particular, particle agglomeration may restrict adsorbed gas access to only the outer surfaces of aggregates, potentially causing an underestimation of the true surface area of primary particles. Consequently, the calculated particle size tends to be larger than the actual size. Furthermore, the particle size obtained from the BET method represents only an average value and does not reflect the full particle size distribution of the sample. When the particle size distribution is broad, smaller particles can fill the voids between larger ones, increasing initial packing density and enhancing diffusion by increasing contact points, which facilitates densification during sintering. Therefore, the relationship between the particle size shown in the figure and the ceramic pore size should be interpreted with caution, as it may be

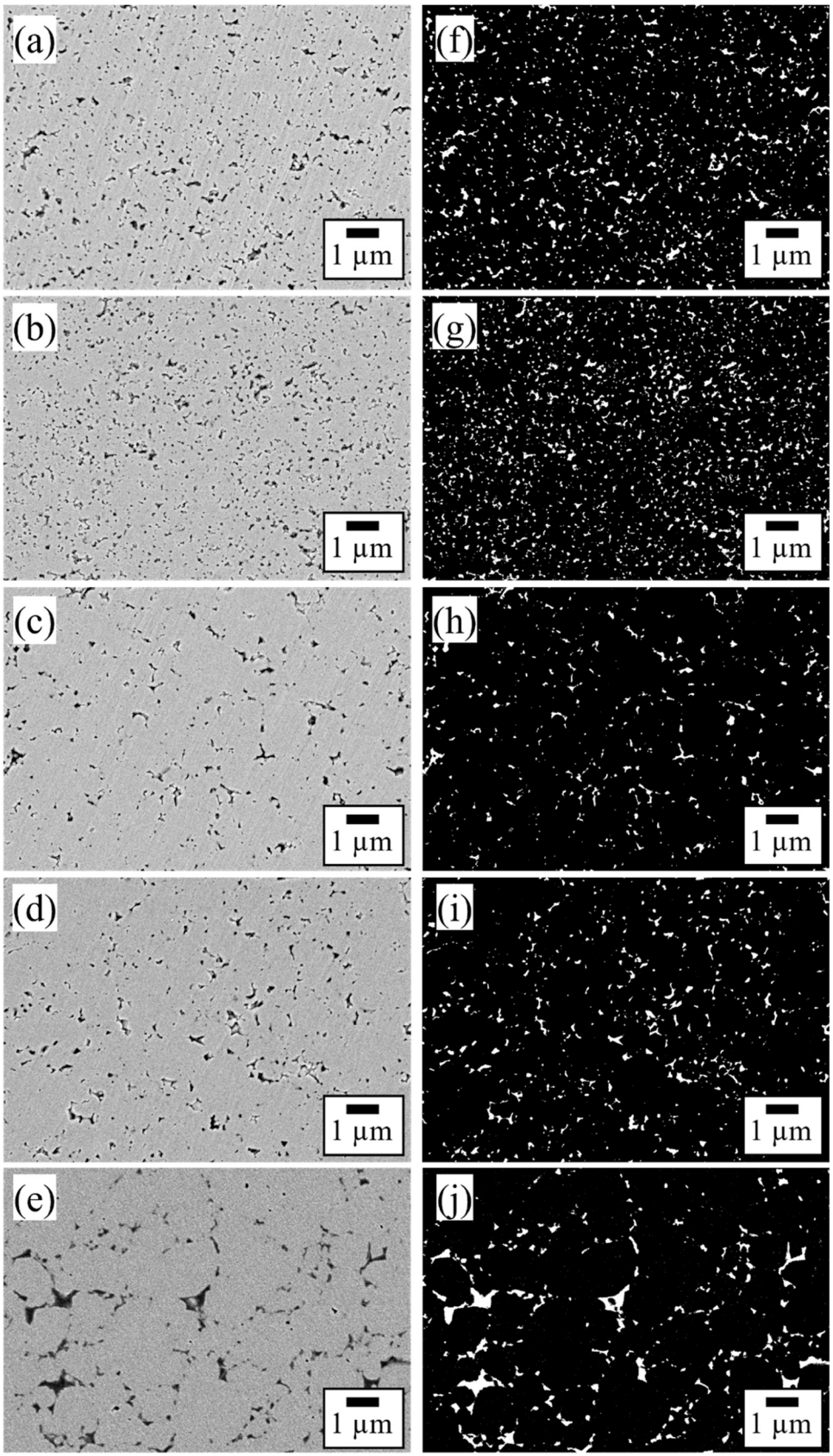

Fig. 6. Cross-sectional FE-SEM images (backscattered electron images) and their binarized images of cryolite ceramics fabricated using raw particles either uncalcined or calcined at various temperatures. The fabrication conditions for the ceramics were fixed at a pressing temperature of 180 °C, pressing pressure of 585 MPa, pressing duration of 10 min, and addition of 10 wt% deionized water. (a) Ceramics using uncalcined raw particles; (b) using particles calcined at 300 °C; (c) at 400 °C; (d) at 500 °C; and (e) at 600 °C. (f), (g), (h), (i), and (j) are binarized images of (a), (b), (c), (d), and (e).

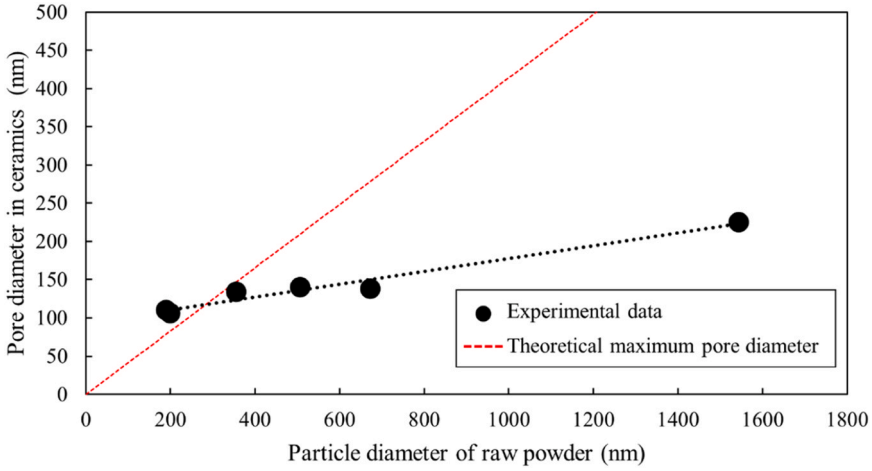

Fig. 7. Relationship between particle diameter of raw cryolite powder and pore diameter in cryolite ceramics (black markers). An approximate trend line is shown as a black dashed line, and the theoretical maximum pore diameter based on H.S. Field's close-packing theory is indicated by a red dashed line.

affected by measurement uncertainties and the influence of the raw powder's particle size distribution.

Next, the IR transmittance of the cryolite ceramics was measured using FTIR spectroscopy. Fig. 8 shows the IR transmission spectra of cryolite ceramics sintered at low temperatures using synthetic cryolite powder. The sintering conditions were as follows: sintering temperature of 180 °C, uniaxial pressure of 585 MPa, duration time of 10 min, and addition of 10 wt% deionized water. The transmittance per millimeter of thickness was calculated according to the Beer-Lambert law, using Equation (iii) [31].

$$T = T_d^{(1/d)} \ldots \quad \text{(iii)}$$

where T is the transmittance per millimeter of thickness, d is the thickness of the sample, and T_d is the measured transmittance of the sample with a thickness of d mm. Samples prepared from uncalcined powder and powders calcined at 300, 400, 450, 500, and 600 °C exhibited thicknesses of 0.916, 0.930, 0.874, 0.905, 0.867, and 0.885 mm, respectively. As a result, cryolite ceramics made from powders calcined at temperatures between 400 and 500 °C exhibited high IR transmittance, with values above 70 % in the 3.8–5.6 μm wavelength range per 1 mm thickness. In both cases, strong absorption peaks attributed to water or hydroxyl groups were observed near the 3 and 6 μm wavelength regions. Cryolite ceramics made from uncalcined powder or powders calcinated at a lower temperature of 300 °C showed stronger absorption due to water or hydroxyl groups compared to those calcined at 400–500 °C, which is likely due to the decrease in water or hydroxyl content with calcination above 400 °C. Cryolite ceramics synthesized from raw powder calcined at 600 °C showed markedly reduced transmittance at shorter wavelengths compared to other samples. This reduction is attributed to increased particle size resulting from higher calcination temperatures, which enlarged pore size and enhanced light scattering. The sample had a median pore diameter of 225 nm, below one-tenth of the mid-infrared wavelength range of 3.8–5.6 μm, yet some pores were larger than one-tenth of the wavelength, potentially leading to light scattering.

Herein, the changes in the IR transmission spectra are discussed using equation (iv), which describes the IR transmittance T(λ) of ceramics while considering the effects of scattering and absorption [32].

$$T(\lambda) = \left(1 - \left(\frac{1 - n_{av}}{1 + n_{av}}\right)^2\right) \times \exp(-\delta(\lambda)t) \ldots \quad \text{(iv)}$$

$$\delta(\lambda) = \alpha(\lambda) + \gamma_p(\lambda) + \gamma_g(\lambda) \ldots \quad \text{(v)}$$

$$\gamma_p(\lambda) = \frac{16\pi^4 d_p^3 \Delta n_p^2 n_{av}^2}{9\lambda^4} V_p \ldots \quad \text{(vi)}$$

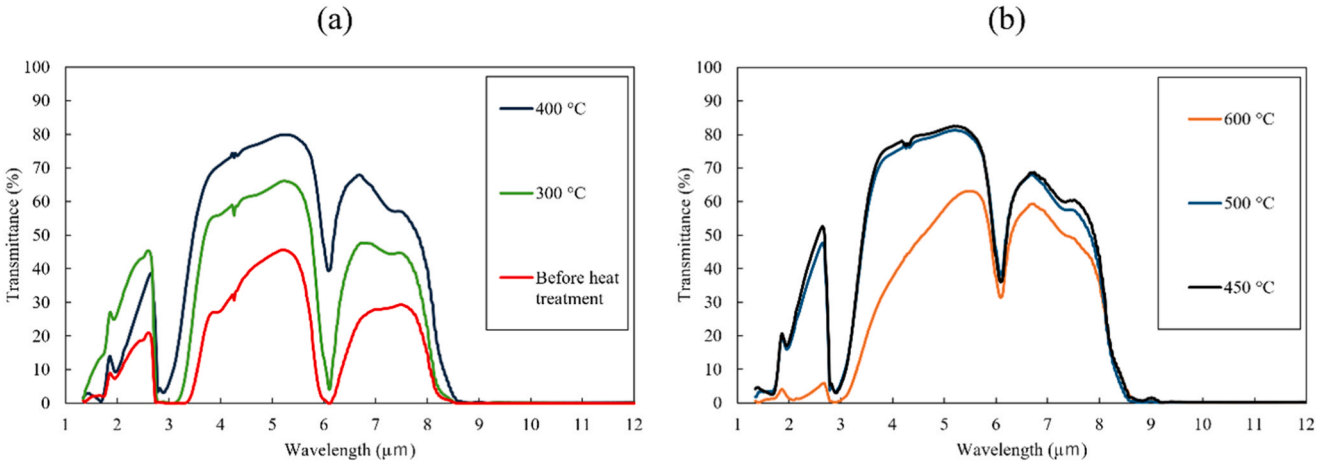

Fig. 8. IR transmittance spectra of synthetic cryolite ceramics produced using raw cryolite particles calcinated at different temperatures: (a) 400 °C or below, and (b) 450 °C or above.

$$\gamma_g(\lambda) = \frac{3\pi^2 d_g \Delta n_g^2}{\lambda^2} V_g \ldots \quad (\text{vii})$$

Conditions for Approximate

$$\pi d_p \ll \lambda \ldots \quad (\text{viii})$$

$$\frac{d_g n_{av} \Delta n_g}{2\pi\lambda} \ll 1 \ldots \quad (\text{ix})$$

In Equation (iv), δ(λ) represents the apparent attenuation coefficient, expressed in equation (v). In equation (v), α(λ) denotes the linear absorption coefficient, $\gamma_p(\lambda)$ indicates the scattering coefficient due to pores, and $\gamma_g(\lambda)$ represents the scattering coefficient due to crystal anisotropy, with $\gamma_p(\lambda)$ and $\gamma_g(\lambda)$ further defined by Equations (vi) and (vii), respectively. Within the equations, n_{av} denotes the average particle refractive index, d_p is the pore diameter, Δn_p represents the refractive index difference between particles and pores, V_p indicates porosity, d_g refers to particle size, Δn_g signifies the refractive index difference due to crystal orientation, and V_g represents the effective volume fraction of particles. It is assumed that equations (iv) through (vii) hold under the approximations given by equations (viii) and (ix). From equations (vi) and (vii), it can be inferred that the scattering coefficient due to pores is inversely proportional to the fourth power of the wavelength, whereas the scattering coefficient due to crystal anisotropy is inversely proportional to the square of the wavelength. Consequently, stronger scattering occurred at shorter wavelengths. When using raw powder with a calcination temperature of 600 °C, a notable decrease in transmittance was observed on the shorter-wavelength side compared to the longer-wavelength side, which was attributed to the increased scattering at shorter wavelengths. Furthermore, equation (vi) indicates that the scattering coefficient due to pores is proportional to the cube of the pore diameter, highlighting the significant impact of the pore size on scattering. Therefore, in the case of the cryolite ceramics studied, larger raw particle sizes resulted in an increase in the pore diameter of the ceramics, ultimately leading to a decrease in transmittance owing to scattering effects.

Additionally, cryolite possesses a monoclinic crystal structure [33] and, as previously mentioned, exhibits extremely low refractive index anisotropy, with Δn approximately 0.0015 or less. Although this small anisotropy may induce slight birefringence, its effect on infrared transmittance in practical applications is negligible. Light scattering intensity is generally inversely proportional to the fourth power of the wavelength and directly proportional to the square of the refractive index difference [32]. Therefore, in the infrared region, characterized by longer wavelengths, the effects of scattering and birefringence are minimal, resulting in an almost negligible reduction in transmittance. In addition, the cryolite ceramics synthesized in this study contained a small amount of $Na_5Al_3F_{14}$, originating from the precursor powder. A slight mismatch in refractive indices between this minor secondary phase and the cryolite matrix may have caused limited light scattering, potentially contributing to a modest reduction in transmittance. Enhancing the phase purity of the starting powder is expected to improve the optical performance of the ceramics.

Fig. 9 presents the TG (a) and DTA (b) curves of powders obtained by grinding low-temperature sintered cryolite ceramics with a mortar. All samples exhibited gradual weight loss and gentle endothermic peaks upon heating. As the calcination temperature of the raw powders increased, the thermal weight loss of the resulting ceramics decreased. This phenomenon is likely due to the reduction of hydroxyl groups and absorbed water in the ceramics following sintering. Unlike the DTA curve of the raw powder shown in Fig. 2(a), no exothermic peaks were observed apart from the gentle endothermic peak. These findings further support the crystallization of secondary phases induced by sintering.

Fig. 10(a) illustrates the relationship between the calcination temperature of the powder and both the transmittance (average value in the 3.8–5.6 μm range) and the relative density. The relative density remained at approximately 90 % irrespective of the calcination temperature, and no significant variations were observed. On the other hand, the transmittance peaked at 79 % for a powder calcination temperature of 450 °C and decreased as the temperature approached either lower or higher values.

Fig. 10(b) presents the relationship between pore diameter in the ceramics and IR transmittance (average value in the 3.8–5.6 μm range). The transmittance reached a maximum at an intermediate pore diameter, suggesting the existence of an optimal pore size that minimizes light scattering.

When the calcination temperature of the raw material particles is 300 °C or lower, adsorbed water and hydroxyl groups are retained, leading to a decrease in the IR transmittance of the ceramics due to absorption. Conversely, at a calcination temperature of 600 °C, pore sizes exceeding 1000 nm, which are close to the IR wavelength, cause a decrease in the IR transmittance of the ceramics due to scattering. As a result, the transmittance remained above 75 % within the range of 400–500 °C for the powder calcination temperature, indicating that this range is favorable for achieving ceramics with a good balance of light absorption and scattering.

Fig. 11 shows the effects of distinct parameter adjustments: (a) uniaxial pressure (fixed at 180 °C, 10 min, 10 wt% water), (b) sintering temperature (fixed at 585 MPa, 10 min, 10 wt% water), (c) duration (fixed at 180 °C, 585 MPa, 10 wt% water), and (d) deionized water content (fixed at 180 °C, 585 MPa, 10 min). These results highlight the impact on transmittance and relative density when varying uniaxial pressure, sintering temperature, duration, and deionized water content, utilizing raw powder material calcined at 450 °C. Thicknesses of samples corresponding to each parameter set were measured as follows: for

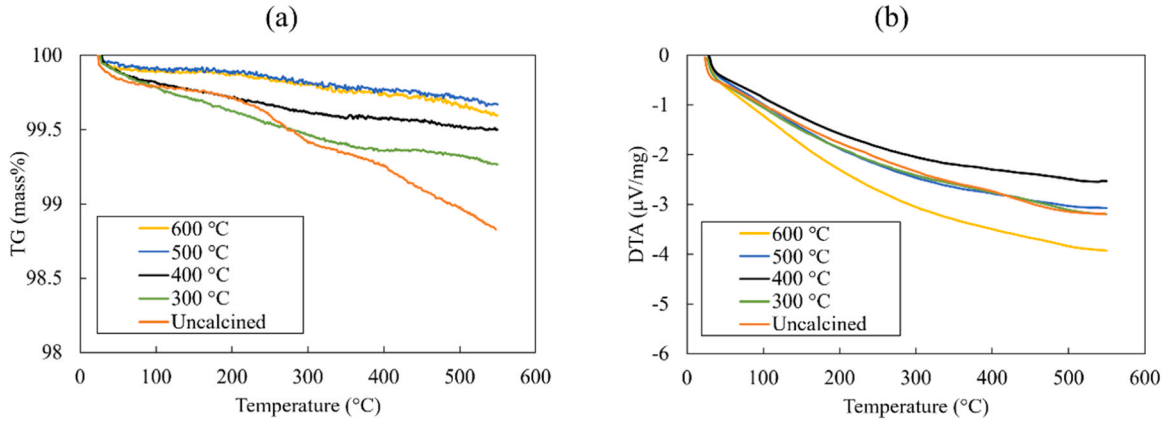

Fig. 9. TG (a) and DTA (b) curves of powders obtained by grinding cryolite ceramics, fabricated via CSP using raw powders either uncalcined or calcined at various temperatures.

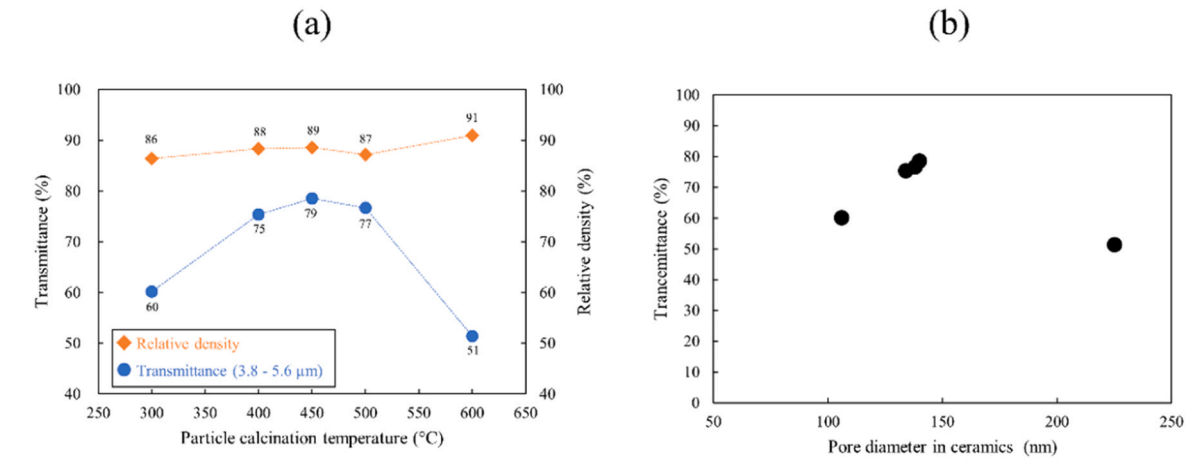

Fig. 10. IR transmittance (average from 3.8 to 5.6 μm) and relative densities of cryolite ceramics as a function of (a) particle calcination temperature and (b) pore diameter in ceramics.

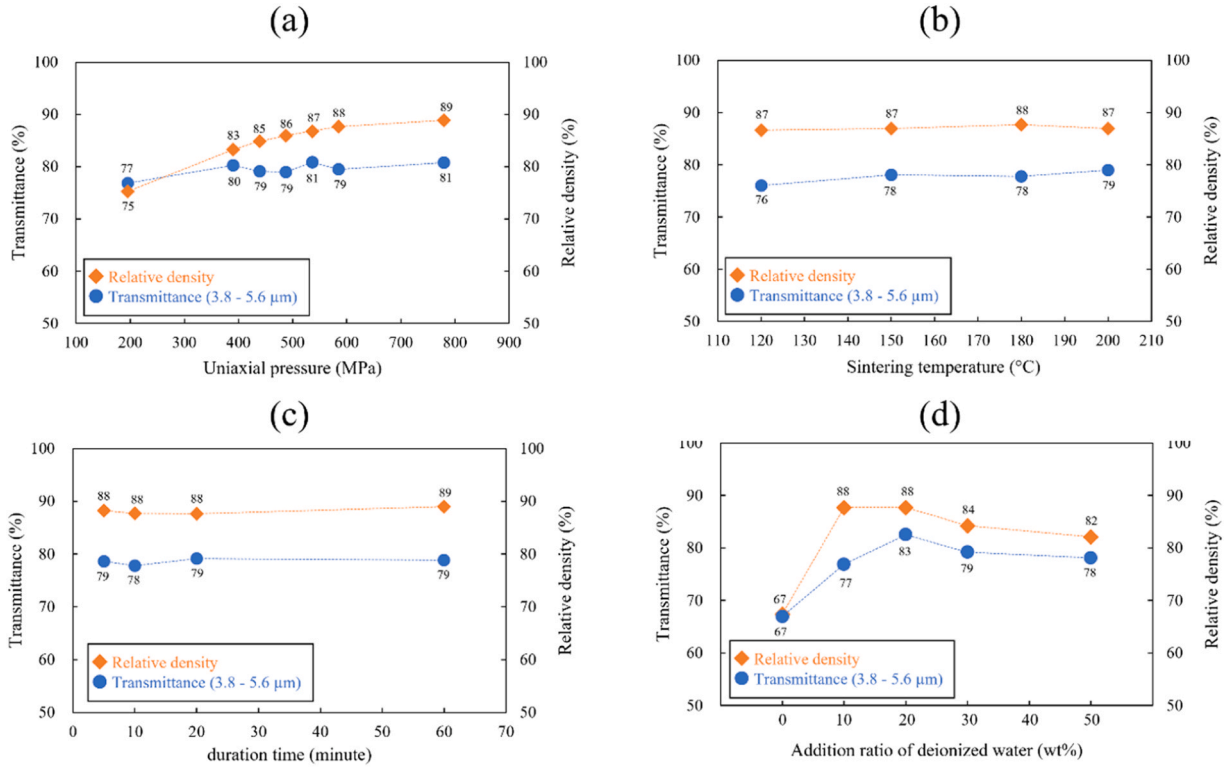

Fig. 11. Variations in transmittance and relative density when altering pressing pressure, pressing temperature, pressing duration, and amount of deionized water added using raw powder material calcinated at 450 °C. (a) uniaxial pressure, (b)sintering temperature, (c) duration time, and (d) amount of deionized water added.

uniaxial pressures of 195, 390, 439, 488, 536, 585, and 780 MPa, thicknesses were 1.07, 0.96, 0.95, 0.94, 0.93, 0.92, and 0.89 mm, respectively. Thicknesses at sintering temperatures of 120, 150, 180, and 200 °C were 0.93, 0.92, 0.92, and 0.92 mm, respectively. For durations of 5, 10, 20, and 60 min, thicknesses were 0.91, 0.92, 0.92, and 0.91 mm, respectively. Thicknesses corresponding to deionized water contents of 0, 10, 20, 30, and 50 wt% were 1.09, 0.91, 0.90, 0.83, and 0.78 mm, respectively.

In Fig. 11(a), within the uniaxial pressure range of 195–780 MPa, both relative density and transmittance increase with higher pressures due to enhanced particle packing, which improves density and reduces scattering by minimizing pores. No notable changes in relative density or transmittance are observed within the sintering temperature range of 120–200 °C and duration times from 5 to 60 min. The addition of 0 wt% deionized water results in significantly lower relative density and transmittance compared to conditions with 10–50 wt% water, likely due to insufficient densification, which leads to larger and more numerous pores that increase scattering and reduce transmittance. Maximum relative density and transmittance are achieved with 20 wt% deionized water, while further increases to 30 wt% and 50 wt% result in reductions in both metrics, as excessive deionized water causes powder to flow out of the mold, impairing pressure transmission to the powder and decreasing relative density and transmittance.

3.3. Effect of deionized water on the densification and IR-transmittance of cryolite ceramics

To investigate the cause of the observed decrease in the relative density and transmittance when deionized water was not added, cross-sectional observations were conducted using FE-SEM. Fig. 12 shows the cross-sectional FE-SEM image and the corresponding binarized image of ceramics synthesized without the addition of deionized water under the conditions of a powder calcination temperature of 450 °C, sintering temperature of 180 °C, uniaxial pressure of 585 MPa, and duration time of 10 min. Even in the ceramics fabricated without the addition of deionized water, the particles were bonded and sintered together. Even without the addition of deionized water, the state was not merely that of a compacted powder body; interparticle bonding was present, suggesting that water was not an absolute necessity for the sintering process. Nonetheless, the samples without deionized water addition exhibited a greater number and size of pores than those with deionized water addition. The equivalent circular diameters of the pores, determined through binarization and image analysis of the SEM images, were 355 nm for the samples without water addition and 140 nm for those with 10 wt% water addition. Furthermore, the relative densities were 67 % and 89 %, respectively, indicating that the addition of water can reduce both the size and quantity of the pores. The addition of deionized water is anticipated to promote particle rearrangement through particle sliding, enhancing the packing density [34], and it has been found to promote densification during the cold sintering process of cryolite. Additionally, the increase in pore diameter and porosity is believed to have contributed to the enhancement of light scattering, which, in turn, resulted in reduced transmittance.

In the cold sintering process of cryolite, interparticle bonding occurred even without the addition of deionized water. This suggests that dissolution in a solvent is not strictly required for bond formation. When deionized water was added, sliding-facilitated particle rearrangement was enhanced, and the mold environment temporarily formed hydrothermal conditions, likely promoting bonding via surface hydroxyl groups and improving densification [35,36]. Even in the absence of added water, the applied pressure may increase particle contact, and localized hydrothermal-like condition was developed at particle interfaces due to adsorbed water. As a result, interparticle bonding may have occurred without the need for external solvent addition.

Previous studies have reported the fabrication of Dy- or Tb-doped Na_3AlF_6 ceramics via spark plasma sintering (SPS) [24,25]. However, these reports did not provide specific data on the density or infrared transmittance of the resulting materials. Some samples exhibited coloration due to carbon contamination from the mold. Although their translucency suggests relatively high density, pore size control was not addressed, which likely limited their optical transparency in the mid-infrared region.

In contrast, the present study demonstrates for the first time the fabrication of cryolite ceramics with high mid-infrared transmittance through cold sintering below 200 °C. This achievement was made possible by systematically controlling both scattering and absorption mechanisms. The ceramics reached a maximum relative density of approximately 90 %. Although this represents a significant result for low-temperature processing, further improvements in transmittance are expected with continued optimization.

One promising approach to enhance transmittance involves optimizing particle packing by adjusting the particle size distribution, such as incorporating larger particles, without increasing the hydroxyl content of the raw powders. This strategy may improve both optical performance and density in future developments.

In this study, we demonstrated that the pore size of ceramics can be regulated by the particle size of raw materials in the low-temperature sintering process of cryolite. While smaller pore sizes can reduce IR scattering, they necessitate the use of smaller raw particles, which leads to decreased IR transmittance due to absorption from adsorbed water and hydroxyl groups. This highlights the importance of achieving a balanced pore size in IR transparent ceramics. These findings will be beneficial for the future application of low-temperature sintering techniques to IR transparent ceramics.

4. Conclusion

Mid-IR transparent cryolite ceramics were successfully fabricated via the cold sintering process conducted below 200 °C. Optimizing the calcination temperature of the raw powder controlled particle size, which effectively suppressed hydroxyl absorption and minimized pore-induced scattering, resulting in ceramics with high mid-IR transmittance and relative density. Although solvent addition is not essential for particle bonding, it facilitates particle rearrangement and densification. This approach not only reduces energy consumption but also advances the development of environmentally friendly optical materials suitable for IR applications. These findings establish a viable and sustainable low-temperature processing route for cryolite ceramics, offering a promising alternative to conventional high-temperature techniques.

CRediT authorship contribution statement

Tohru Sekino: Writing – review & editing, Supervision, Methodology, Conceptualization. **Natsuki Sato:** Writing – review & editing, Writing – original draft, Methodology, Investigation, Formal analysis, Conceptualization. **Tatsuro Yoshioka:** Writing – review & editing, Validation, Methodology, Investigation, Formal analysis. **Yeongjun Seo:** Writing – review & editing, Validation, Methodology, Investigation, Conceptualization. **Tomohiro Kitagaki:** Writing – review & editing, Investigation, Formal analysis. **Sunghun Cho:** Writing – review & editing, Investigation, Formal analysis. **Tomoyo Goto:** Writing – review & editing, Methodology, Investigation.

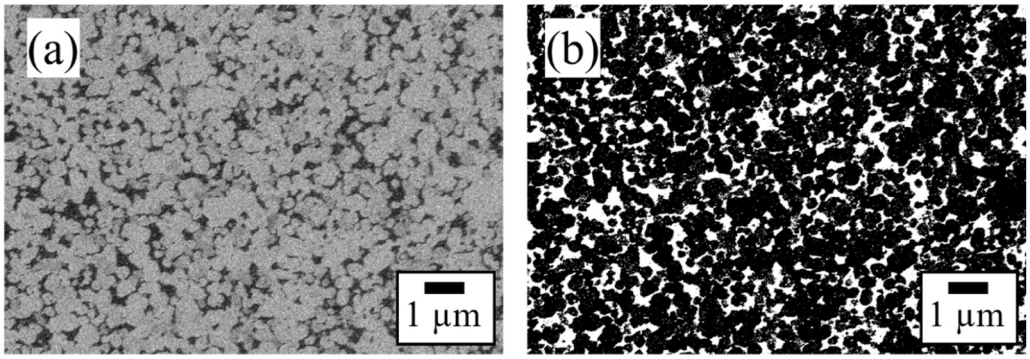

Fig. 12. Cross-sectional FE-SEM image (a) and binarized image (b) of cryolite ceramics synthesized without addition of deionized water.

Funding

This research did not receive any specific grant from funding agencies in the public, commercial, or not-for-profit sectors.

Declaration of Competing Interest

The authors declare that they have no known competing financial interests or personal relationships that could have appeared to influence the work reported in this paper.

Acknowledgements

The authors thank Mr. Ryosuke Sawa and Mr. Naoki Kurizoe of Panasonic Corporation, Japan for the useful comments and suggestions.

References

[1] S.S. Ballard, Infrared optical materials, old and new, Jpn. J. Appl. Phys. 3 (1964) 23–29, https://doi.org/10.7567/JJAPS.1S1.23.
[2] E.F. McCoy, R. St, C. Smart, Infrared spectra from reflection studies of carbon monoxide on evaporated nickel films, Surf. Sci. 39 (1973) 109–120, https://doi.org/10.1016/0039-6028(73)90098-8.
[3] B. Cockayne, M. Chesswas, D.B. Gasson, Single-crystal growth of sapphire, J. Mater. Sci. 2 (1967) 7–11, https://doi.org/10.1007/BF00550046.
[4] E.S. Sajda, B.W. Kippenhan, W.H. White, Epitaxial growth of silicon, IBM J. Res. Dev. 4 (1960) 288–295, https://doi.org/10.1147/rd.43.0288.
[5] J.G.J. Peelen, R. Metselaar, Light scattering by pores in polycrystalline materials: transmission properties of alumina, J. Appl. Phys. 45 (1974) 216–220, https://doi.org/10.1063/1.1662961.
[6] R.J. Bratton, Translucent sintered $MgAl_2O_4$, J. Am. Ceram. Soc. 57 (1974) 283–286, https://doi.org/10.1111/j.1151-2916.1974.tb10901.x.
[7] Y. Yamaguchi, The development of low-temperature sintering techniques for functional ceramic devices using chemical reactions, J. Ceram. Soc. Jpn. 128 (2020) 747–755, https://doi.org/10.2109/jcersj2.20107.
[8] Y. Nakashima, H.R. Khosroshahi, C. Takai, M. Fuji, Non-firing ceramics: activation of silica powder surface for achieving high-density solidified bodies, Adv. Powder Technol. 29 (2018) 1900–1903, https://doi.org/10.1016/j.apt.2018.04.029.
[9] S. Ueno, Y. Sakamoto, K. Nakashima, S. Wada, Low-temperature fabrication of titanium metal/barium titanate composite capacitors via hydrothermal method and their dielectric properties, J. Ceram. Soc. Jpn. 122 (2014) 447–451, https://doi.org/10.2109/jcersj2.122.447.
[10] D.J. Guo, D.H. Guo, A.L. Baker, M.T. Lanagan, E.R. Kupp, G.L. Messing, C. A. Randall, Cold sintering: a paradigm shift for processing and integration of ceramics, Angew. Chem. 128 (2016) 11629–11633, https://doi.org/10.1002/ange.201605443.
[11] N. Guo, G. Zhu, H. Xu, X. Jiang, X. Zhang, J. Song, Y. Zhao, L. Jiang, Y. Zhang, Q. Wang, S. Long, T. Wei, A. Yu, Preparation of CaF_2 transparent ceramics by cold sintering, Ceram. Int. 48 (2022) 34184–34189, https://doi.org/10.1016/j.ceramint.2022.08.339.
[12] B. Liu, K. Sha, Q.W. Zhou, K.X. Song, F. Shi, Y.H. Cheng, One-step cold sintering process towards translucent BaF_2 ceramics, J. Eur. Ceram. Soc. 43 (2023) 7053–7058, https://doi.org/10.1016/j.jeurceramsoc.2023.07.008.
[13] B. Liu, F.L. Lin, C.C. Hu, K.X. Song, J.H. Zhang, C. Lu, Y.H. Huang, Novel transparent LiF ceramics enabled by cold sintering at 150 °C, Scr. Mater. 220 (2022) 114917, https://doi.org/10.1016/j.scriptamat.2022.114917.
[14] B. Gordon, M. Barrow, The intensities of infrared hydroxyl bands, J. Phys. Chem. 59 (1955) 1129–1132, https://doi.org/10.1021/j150533a003.
[15] H.A. Benesi, A.C. Jones, An infrared study of the water-silica gel system, J. Phys. Chem. 63 (1959) 179–182, https://doi.org/10.1021/j150572a012.
[16] T.H. Beauvoir, C. Estournès, Translucent γ-AlOOH and γ-Al_2O_3 glass-ceramics using the cold sintering process, Scr. Mater. 194 (2021) 113650, https://doi.org/10.1016/j.scriptamat.2020.113650.
[17] H.T. Horsfield, The strength of asphalt mixtures, J. Soc. Chem. Ind. 53 (1934) 107–115, https://doi.org/10.1002/jctb.5000531605.
[18] C. Zhu, S. Zhou, Y. Wei, B. Li, H. Wang, Recovery of fluoride from spent cathode carbon block by combustion combined with water leaching process, J. Clean. Prod. 408 (2023) 137229, https://doi.org/10.1016/j.jclepro.2023.137229.
[19] M. Li, S. Zhou, B. Li, Y. Wei, H. Wang, Migration of fluorine during the reduction of copper slag from spent cathode carbon produces copper–iron alloys, J. Mater. Sci. Technol. 23 (2023) 1821–1833, https://doi.org/10.1016/j.jmrt.2023.01.145.
[20] S.F. Parker, A.J. Ramirez-Cuesta, L.L. Daemen, The structure and vibrational spectroscopy of cryolite, Na_3AlF_6, RSC Adv. 10 (2020) 25856–25863, https://doi.org/10.1039/D0RA04804F.
[21] H.Y. Fan, Infra-red absorption in semiconductors, Rep. Prog. Phys. 19 (1956) 107–155, https://doi.org/10.1088/0034-4885/19/1/304.
[22] P.A. Forser JR, Phase equilibria in the system Na_3AlF_6—AlF_3, J. Am. Ceram. Soc. 53 (1970) 598–600, https://doi.org/10.1111/j.1151-2916.1970.tb15980.x.
[23] H. Pauly, Cryolite, chiolite and cryolithionite: optical data redetermined, Bull. Geol. Soc. Den. 26 (1977) 95–101, https://doi.org/10.37570/bgsd-1976-26-07.
[24] H. Sakaguchi, H. Fukushima, T. Kato, D. Nakauchi, N. Kawaguchi, Y. Yanagida, Dosimetric properties of Dy-doped Na_3AlF_6 ceramics synthesized by spark plasma sintering method, J. Mater. Sci. Mater. Electron 34 (2023) 1661, https://doi.org/10.1007/s10854-023-11050-0.
[25] H. Sakaguchi, H. Fukushima, T. Kato, D. Nakauchi, N. Kawaguchi, T. Yanaghida, Photoluminescence and dosimetric properties of Tb-doped Na_3AlF_6 ceramics, J. Lumin 254 (2023) 119533, https://doi.org/10.1016/j.jlumin.2022.119533.
[26] I. Sevonkaev, D.V. Goia, E. Matijević, Formation and structure of cubic particles of sodium magnesium fluoride (neighborite), J. Colloid Interf. Sci. 317 (2008) 130–136, https://doi.org/10.1016/j.jcis.2007.09.036.
[27] J.M. Pappas, A.R. Thakur, X. Dong, Effects of zirconia doping on additively manufactured alumina ceramics by laser direct deposition, Mater. Des. 192 (2020) 108711, https://doi.org/10.1016/j.matdes.2020.108711.
[28] F.J. Parry A, Melting point of cryolite, J. Am. Ceram. Soc. 51 (1968) 107–109.
[29] S.H. Min, A study on analysis of particle size distribution, Arch. Pharm. Res 3 (1980) 65–74, https://doi.org/10.1007/BF02855805.
[30] M. Suzuki, T. Oshima, H. Ichiba, I. Hasegawa, Void fraction of multi-component randomly packed beds with size distributions, Kagaku Kogaku Ronbunshu 11 (1985) 438–443, https://doi.org/10.1252/kakoronbunshu.11.438.
[31] M. ihara, T. Yamamoto, Spectrophotometric study of coloured glasses(1) spectrophotometric study of glasses coloured by iron and manganese, J. Ceram. Assoc. Jpn. 66 (1958) 144–152, https://doi.org/10.2109/jcersj1950.66.750_144.
[32] H. Furuse, N. Horiuchi, B.N. Kim, Transparent non-cubic laser ceramics with fine microstructure, Sci. Rep. 9 (2019) 10300, https://doi.org/10.1038/s41598-019-46616-8.
[33] E.G. Steward, H.P. Rooksby, Transitions in crystal structure of cryolite and related fluorides, Acta Crystallogr 6 (1953) 49–52, https://doi.org/10.1107/S0365110X53000107.
[34] H. Guo, A. Baker, J. Guo, C.A. Randall, Protocol for ultralow-temperature ceramic sintering: an integration of nanotechnology and the cold sintering process, ACS Nano 10 (2016) 10606–10614, https://doi.org/10.1021/acsnano.6b03800.
[35] H. Guo, A. Baker, J. Guo, C.A. Randall, Cold sintering process: a novel technique for low-temperature ceramic processing of ferroelectrics, J. Am. Ceram. Soc. 99 (2016) 3489–3507, https://doi.org/10.1111/jace.14554.
[36] A. Prathan, J. Sanglao, T. Wang, C. Bhoomanee, P. Ruankham, A. Gardchareon, D. Wongratanaphisan, Controlled structure and growth mechanism behind hydrothermal growth of TiO_2, Nanorods. Sci. Rep. 10 (2020) 8065, https://doi.org/10.1038/s41598-020-64986-6.